# Synthesis and adsorption study of NiO nanobelts for removal of anionic dyes

Yi-Biao Shao, Jian-Hua Huang*

*Department of Chemistry, Zhejiang Sci-Tech University, Hangzhou 310018, China, Tel. +86 57186843228;
emails: jhhuang@zstu.edu.cn (J.-H. Huang), 287172973@qq.com (Y.-B. Shao)*

### ABSTRACT

NiO nanobelts with 40–90 nm in width and several tens of micrometer in length were synthesized by a hydrothermal reaction and subsequent calcination. They possessed high specific surface area of 102.4 $m^2$/g and behaved as an efficient adsorbent for removal of anionic dyes including methyl blue (MB; 1,996 mg/g), methyl orange (MO) (1,291 mg/g), and Congo red (CR) (331 mg/g). The adsorption kinetics and adsorption mechanism were investigated systematically. The adsorption for MB was well represented by Langmuir isotherm model, while the adsorption kinetics was well described by the pseudo-second-order model. Fourier transform infrared studies revealed that the good adsorption capacity for anionic dyes could be largely attributed to the electrostatic attraction between $SO_3^-$ group in dye molecule and positively charged surface of NiO. Our NiO nanobelts showed much higher adsorption capacity for MO and CR compared with other transition metal oxides and NiO nanosheets reported previously. Our product is expected to be promising material for wastewater treatment.

*Keywords:* Adsorption; NiO; Organic dyes; Electrostatic interaction

## 1. Introduction

With the rapid development of industry, large amounts of chemicals are discharged into aqueous environment; water pollution is thus becoming more and more serious. Among various water pollutions, organic dye pollution is of awfulness [1]. In addition to affecting the aquatic ecosystems, organic dyes may bring a chief threat to human health due to their toxic, mutagenic, and carcinogenic substances. Meanwhile, they have high stability to temperature, light, and many chemicals. Therefore, it is important to remove organic dyes from wastewater [2,3].

Adsorption has been shown to be an effective and promising method to remove organic dyes from water because of its simplicity and flexibility in design and operation [2–4]. Many adsorbents have been reported for removal of some common dyes. Among them, carbon-based materials, such as graphene, multi-walled carbon nanotube, and porous carbon, have received considerable attention due to their low density, stability, and suitability for large-scale production [5–7]. Chitosan-based adsorbents have also attracted particular interests due to their environmental-friendly properties, high availability, and versatility [8,9].

In recent years, metal oxides have attracted much attention in the field of adsorption due to their cheapness, high stability, and easy separation [10]. Various organic dyes can be removed effectively by metal oxides from aqueous solution. For example, amorphous Fe, Co, and Ni oxides showed excellent adsorption capacity for removal of methyl blue (MB). However, their adsorption capacities for methyl orange (MO) were only 9.73, 11.53, and 129.45 mg/g, respectively [11]. Similarly, mesoporous NiO microspheres had an adsorption capacity of 164.7 mg/g for MO [12]. ZnO nanoparticles showed excellent adsorption performance for MB. While their adsorption capacity for MO, Rhodamine B (RhB), and methylene blue (MYB) solutions was negligible [13]. The X-ray photoelectron spectroscopy (XPS) analysis confirmed that the adsorption of MB onto ZnO nanoparticles mainly originated from the ionic bonding between $Zn^{2+}$ in $Zn(OH)^+$ and sulfonic groups in MB molecule [13]. Yang et al. [14] found that $MnFe_2O_4$ could

* Corresponding author.

remove MB and Congo red (CR) simultaneously. The authors pointed out that the dye adsorption was caused by the hydrogen bond and van der Waals interaction [14]. Mesoporous $TiO_2$ was found to be an effective adsorbent for MO. However, the adsorption percentage of MO decreased markedly from 89% to <20% after one adsorption–regeneration cycle [15].

In the present work, NiO nanobelts were synthesized by a simple, template-free hydrothermal reaction and subsequent calcination at 350°C in air. They exhibited excellent adsorption for anionic dyes including MB, MO, and CR. The detailed adsorption properties of NiO nanobelts for MB, including the adsorption mechanism, adsorption kinetics, and regeneration ability, were investigated.

## 2. Experimental

### 2.1. Chemicals

All chemicals used in this work were of analytical grade and used as received without further purification. All solutions were prepared with deionized water. $NiSO_4 \cdot 6H_2O$ and $NH_3 \cdot H_2O$ were purchased from Sinopharm Chemical Reagent Co., Ltd., China. MB and MO was produced by Sigma-Aldrich Chemical Reagent and purchased from Energy Chemical, China. CR and MYB were purchased from Tianjin YongDa Chemical Reagent, China. And RhB was from Shanghai YuanHang Chemical Reagent, China.

### 2.2. Synthesis of NiO nanobelts

NiO nanobelts were synthesized through two steps: (1) production of $\alpha$-$Ni(OH)_2$ and (2) subsequent calcination at 350°C. At the first step, $\alpha$-$Ni(OH)_2$ nanobelts were synthesized by a hydrothermal method similar to reference [16]. In a typical reaction, 1.052 g $NiSO_4 \cdot 6H_2O$ was first dissolved in 60 mL deionized water. Then 4 mL $NH_3 \cdot H_2O$ (2 M) was added dropwise under magnetic stirring. After stirring for 10 min, the solution was transferred to a 100-mL Teflon-lined autoclave and heated at 180°C for 72 h. After naturally cooled down to room temperature, green precipitate was collected by centrifugation, and washed thoroughly with deionized water and ethanol, and then dried at 80°C for 12 h. At the second step, NiO nanobelts were obtained by calcination of the as-prepared $\alpha$-$Ni(OH)_2$ nanobelts at 350°C for 4 h in a muffle furnace.

### 2.3. Characterization

X-ray diffraction (XRD) measurements were conducted on a DX-2700 X-ray diffractometer (Dandong Fangyuan Instrument Co., Ltd., China) using Cu Kα radiation ($\lambda$ = 0.15418 nm). Nitrogen adsorption–desorption isotherms were carried out at –196°C using a Micromeritics ASAP 2020 analyzer. Fourier transform infrared (FT-IR) spectra were recorded on a BRUKER VERTEX 70 infrared spectrophotometer using KBr pellet. Scanning electron microscope (SEM) images were taken with a field emission scanning electron microscope (FE-SEM GEMINI ULTRA 55). Transmission electron microscope (TEM) and higher-resolution transmission electron microscope (HRTEM) images were obtained with a JEOL JEM-2100 TEM equipped with an energy-dispersive X-ray (EDX) spectrometer. XPS measurement was performed on a Kratos AXIS Ultra DLD instrument.

### 2.4. Adsorption equilibrium and kinetic experiments

The adsorption performance of NiO nanobelts was evaluated by removal of organic dyes including MB, MO, CR, RhB, and MYB from aqueous solution at 25°C. As an example, the adsorption isotherm experiment of MB was carried out as follows: a series of MB aqueous solutions with different concentrations of 300–1,500 mg/L were first prepared, then 0.02 L MB aqueous solution, and 0.01 g NiO were added into 0.1 L conical flasks. Afterward, they were sealed, moved to a thermostatic shaker (ZD-85, SHUANGHUA (Jiangsu) Instrument Co., Ltd., China), and kept under a shaking speed of 150 rpm at natural pH (7.0–9.0). After shaking for 12 h, the conical flasks were taken from the shaker, and NiO was separated by centrifugation. The residual MB concentration in supernatant was analyzed by using an UV-Vis spectrometer (UV-4802, UNIC (Shanghai) Instrument Co., Ltd., China) at the maximum absorbance wavelength of MB (590 nm).

The equilibrium adsorption capacity was calculated by:

$$Q_e = (C_0 - C_e) \times V / m \tag{1}$$

where $C_0$ and $C_e$ were the initial and equilibrium concentrations of dye solution (mg/L), respectively. $V$ was the volume of the dye solution (L), and $m$ was the mass of NiO (g).

The adsorption kinetic experiment was basically the same as the adsorption isotherm experiment. Specially, ten conical flasks containing 0.01 g NiO and 0.02 L MB solution (300 mg/L) at natural pH were sealed and shaken in the thermostatic shaker at 25°C. At every preset time interval, one conical flask was taken out from the shaker, and the residual concentration of MB was measured. The adsorption amount at time $t$ was calculated by:

$$Q_t = (C_0 - C_t) \times V / m \tag{2}$$

In order to evaluate the possibility of regeneration and reusability of NiO nanobelts as an adsorbent, five consecutive recycling adsorption experiments were carried out under the same experimental condition with the initial MB concentration 300 mg/L. After an adsorption process, NiO nanobelts were separated by centrifugation, and washed repeatedly with ethanol and deionized water under stirring for 30 min, and then dried at 80°C overnight for the next recycling adsorption, similar to reference [17]. The concentration of residual MB after each adsorption cycle was measured by the same method as described above.

To study the selective adsorption of NiO nanobelts, two other anionic dyes (CR and MO) and two cationic dyes (RhB and MYB) were additionally selected as pollutants. The adsorption experiment was performed under the same condition as that of MB. The residual dye concentration was analyzed by measuring the absorbance at its maximum absorbance wavelength.

## 3. Results and discussion

### 3.1. Characterization of NiO

Fig. 1(a) shows the XRD pattern of the hydrothermal product. The diffraction peaks match well with those of the reported Paraotwayite-type $\alpha$-$Ni(OH)_2$ (JCPDS No. 41-1424).

All the diffraction peaks are sharp and high intensity, indicating the high crystallinity of the Paraotwayite-type α-Ni(OH)$_2$. It is known that the α-phase consists of a hydrotalcite-like structure, having the composition Ni(OH)$_{1.7}$(SO$_4$)$_{0.15}$(H$_2$O)$_{0.79}$ [18], Ni(OH)$_{1.66}$(SO$_4$)$_{0.17}$(H$_2$O)$_{0.29}$ [19], Ni(OH)$_{1.64}$(SO$_4$)$_{0.18}$ (H$_2$O)$_{0.3}$ [20], or Ni(SO$_4$)$_{0.3}$(OH)$_{1.4}$ [21]. However, to reveal the detailed structural information of the as-synthesized α-Ni(OH)$_2$ requires structural refinement of high-quality XRD data, which is difficult for us at this stage. In the present work, we thus focus on the adsorption property of NiO, which is obtained by calcination of α-Ni(OH)$_2$.

After calcination at 350°C, cubic NiO (JCPDS No. 04-0835) was obtained. The formation of the cubic NiO is revealed by the diffraction peaks at 37.28°, 43.30°, and 62.92° corresponding to (111), (200), and (220) main crystal planes [16], respectively (see Fig. 1(b)). The broad diffraction peaks suggest that the cubic NiO is composed of nanoparticles, and the average nanocrystallite size is about 10.5 nm calculated by using Scherrer equation.

In addition, the EDX analysis shows three peaks for the elements Ni, O, and S in the cubic NiO, in addition to the Cu derived from the copper TEM grid (see the inset in Fig. 1(b)).
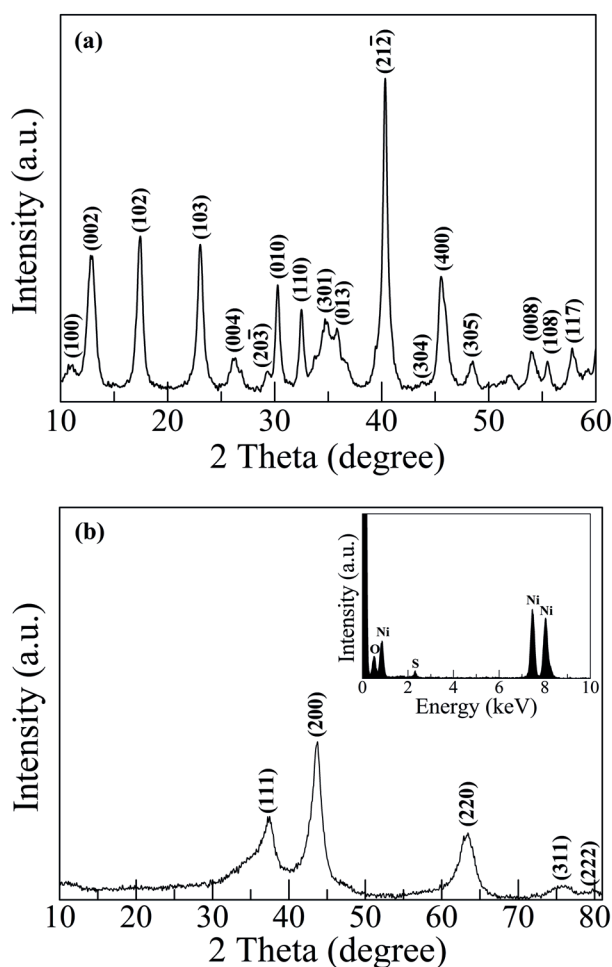


Fig. 1. XRD pattern of (a) the hydrothermal product and (b) the subsequent calcination product obtained at 350°C. Inset in (b) is the EDX spectrum of the calcination product.

It implies that sulfate anions in α-Ni(OH)$_2$ are not completely decomposed after calcination. The residual sulfur is about 3.3% by atomic ratio. Gao and Jelle [20] found that the decomposition of sulfate anions was not completed even at 800°C.

To further insight into the chemical composition and chemical state of the cubic NiO produced by calcining α-Ni(OH)$_2$ at 350°C, XPS analysis was carried out. The XPS survey spectrum presented in Fig. 2(a) demonstrates that the cubic NiO is mostly composed of Ni and O elements. It also indicates the existence of C and S elements in the sample. The peak of C is resulted from the adsorption of CO$_2$ on the sample surface. The weak peak of S element implies that sulfate anions in α-Ni(OH)$_2$ have not been completely decomposed after calcination at 350°C. The S content is determined to be about 3.7% by atomic ratio, in agreement with the EDX result.

For the Ni 2p spectrum shown in Fig. 2(b), there are two regions representing the Ni 2p$_{3/2}$ (850–865 eV) and Ni 2p$_{1/2}$ (870–885 eV) spin–orbit levels, respectively. The binding energies at 855.2 and 872.7 eV are assigned to the Ni 2p$_{3/2}$ and Ni 2p$_{1/2}$ peaks, respectively. Characteristic "shake up" satellites of Ni$^{2+}$ (860.8 eV and 878.6 eV) are clearly observed on the high binding energy side of the main Ni 2p peaks [22]. The energy separation between Ni 2p$_{3/2}$ and Ni 2p$_{1/2}$ peaks is about 17.5 eV, which is in agreement with the reported value of NiO crystal [23]. Fig. 2(c) shows the high-resolution XPS spectrum of S in the 2p region. The S 2p binding energy at 168.2 eV can be assigned to sulfate species [24–26]. However, details of the sulfur-related residuals deserve further study in the future.

Fig. 3(a) shows SEM image of α-Ni(OH)$_2$. We can see that the α-Ni(OH)$_2$ has belt-like morphology with several tens of micrometer in length and 50–100 nm in diameter. The belt surface is quite smooth. After calcination at 350°C for 4 h, the belt-like morphology remains, but the diameter of nanobelt is shrunk for a little (see Fig. 3(b)). Fig. 3(c) shows a typical TEM image of NiO nanobelts, which is in good agreement with SEM observation. From the HRTEM image shown in Fig. 3(d), we observe that the lattice spacing is 0.24 nm, corresponding to the (111) plane of cubic NiO. Based on the above results of XRD, XPS, and HRTEM measurements, we conclude that the Ni element exists in the form of NiO instead of Ni or NiO$_x$ nanoparticles.

### 3.2. Adsorption performance for MB

#### 3.2.1. Effect of calcination temperature

We first studied the effect of the calcination temperature on the equilibrium adsorption capacity $Q_e$ of NiO nanobelts for MB with an initial concentration of 1,500 mg/L. The results are presented in Fig. 4(a). Apparently, $Q_e$ increases with the calcination temperature and reaches the maximum value of 1,996 mg/g for NiO nanobelts obtained at 350°C. Then, it decreases with a further increase in the calcination temperature. Generally, the surface area of an adsorbent is considered to be an important factor to influence its adsorption capacity. The adsorption capacity is usually proportional to its surface area, since a larger surface area can offer more adsorption active sites. Therefore, the specific surface areas of α-Ni(OH)$_2$ nanobelts and its calcination products obtained at different temperatures were determined by performing N$_2$ adsorption–desorption
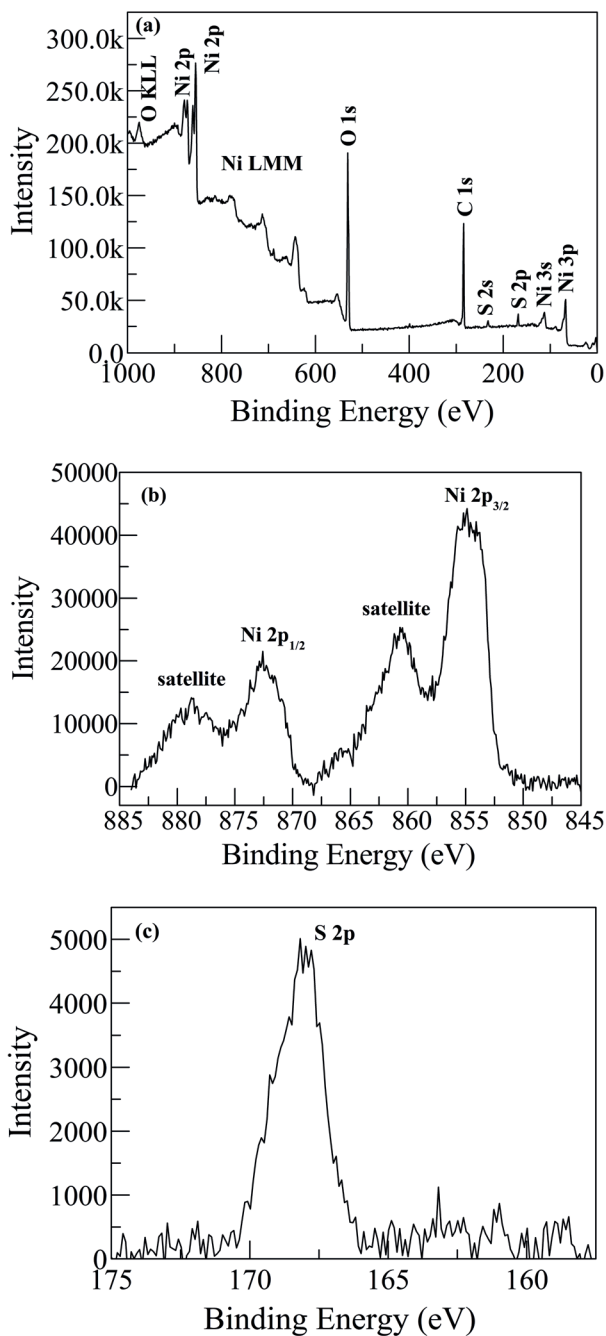
Fig. 2. (a) XPS survey spectrum and high-resolution XPS spectrum of: (b) Ni 2p region and (c) S 2p region of the sample obtained by calcination at 350°C.

measurement. All samples possess type IV isotherm with a H3-type hysteresis loop, indicating the existence of interparticle mesoporosity and macropores [27]. As an example, Fig. 4(b) presents the $N_2$ adsorption–desorption isotherm of NiO nanobelts obtained at 350°C. The specific surface area $S_{BET}$ is calculated by using the Brunauer-Emmett-Teller (BET) method and shown in Fig. 4(a). Clearly, $S_{BET}$ increases with the calcination temperature and reaches the maximum value of 102.4 $m^2$/g at 350°C. However, it drastically decreases with further
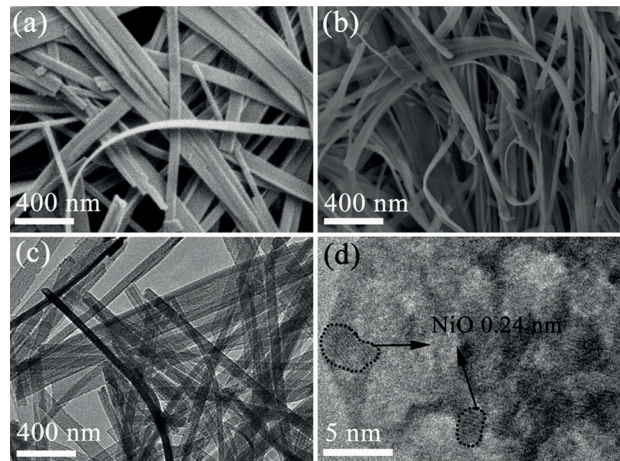


Fig. 3. (a) SEM image of α-Ni(OH)$_2$, and (b) SEM, (c) TEM and (d) HRTEM image of NiO.

increase in the calcination temperature maybe due to the crystal growth. In the following, NiO nanobelts obtained at 350°C were chosen as the adsorbent to investigate the adsorption removal of dyes from aqueous solution, including the adsorption isotherm, adsorption kinetics, and recyclability.

### 3.2.2. Adsorption isotherm

The adsorption isotherm illustrates the adsorption amount of MB at different equilibrium concentrations. Fig. 5 shows the adsorption isotherm of MB onto NiO nanobelts. The equilibrium adsorption capacity $Q_e$ first increases rapidly with an increase in the MB concentration; then it gradually slows down and ultimately reaches the asymptotic value. We find the asymptotic value is roughly equal to the maximum adsorption capacity $Q_{max}$ = 1,996 mg/g. It is much higher than that of some reported adsorbents (see Table 1). But in a very recent paper, a super adsorption capability of amorphous CoO and NiO, synthesized by special laser irradiation, for MB were reported.

In order to understand the adsorption potential between NiO and MB, Langmuir and Freundlich adsorption isotherms are adopted to analyze the experimental data. The Langmuir isotherm is based on the following assumption [15]: (1) the adsorption takes place on homogeneous sites within the adsorbent; (2) each site can hold only one adsorbate molecule; and (3) there is no interaction between adsorbate molecules. It is usually expressed as:

$$Q_e = Q_{max} k_L C_e / (1 + k_L C_e) \tag{3}$$

which can be rearranged in a linear form:

$$C_e / Q_e = 1 / (Q_{max} k_L) + C_e / Q_{max} \tag{4}$$

$Q_{max}$ and the Langmuir equilibrium constant $k_L$ (L/mg) can be calculated from the slope and the intercept of the linear plot of $C_e/Q_e$ vs. $C_e$, respectively. Based on our experimental data, we get the calculated $Q_{max}$ = 2,039 mg/g, $k_L$ = 0.0311 L/mg, and the correlation coefficients $R^2$ = 0.999.
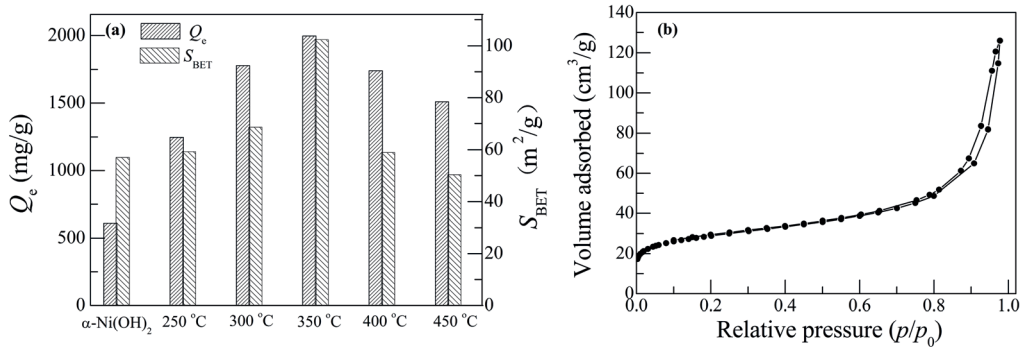
Fig. 4. (a) The equilibrium adsorption capacity $Q_e$ and specific surface area $S_{BET}$ of α-Ni(OH)$_2$ nanobelts and NiO nanobelts obtained at different calcination temperatures: the initial MB concentration $C_0 = 1,500$ mg/L and (b) the N$_2$ adsorption–desorption isotherm of NiO nanobelts obtained by calcination at 350°C.
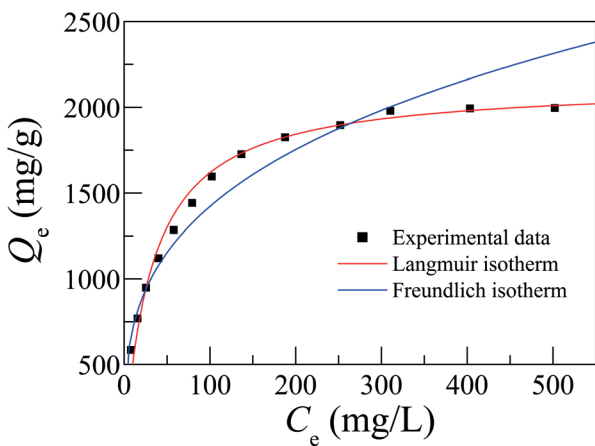


Fig. 5. Comparison of the equilibrium isotherm between experimental data and theoretical model: the initial MB concentration $C_0 = 300\sim1,500$ mg/L.

The Freundlich model assumes that the adsorption takes place on heterogeneous surface [29]. It is expressed by:

$$Q_e = k_F C_e^{1/n} \tag{5}$$

with a linear form:

$$\ln Q_e = \ln k_F + 1/n \ln C_e \tag{6}$$

where $k_F$ (mg/g.(L/mg)$^{1/n}$) is the Freundlich equilibrium constant, and $n$ is an empirical parameter related to the surface heterogeneity or adsorption intensity. $k_F$ and $1/n$ can be determined from the intercept and slope of linear plot of $\ln Q_e$ against $\ln C_e$, respectively. We get $k_F = 353.80$ mg/g.(L/mg)$^{1/n}$, $n = 3.31$, and the correlation coefficients $R^2 = 0.954$.

The fitting results of Langmuir and Freundlich model are also illustrated in Fig. 5. Clearly, Langmuir model yields a better fitting for the experimental data, indicating the homogeneous nature of NiO surface and the monolayer coverage of MB molecule on the surface of NiO nanobelt.

Table 1
Comparison of the adsorption capacity of MB onto some reported adsorbents

| Adsorbent | $Q_{max}$ (mg/g) | References |
|---|---|---|
| NiO | 1,996 | This work |
| Activated charcoal | 25.1 | [6] |
| Magnetic chitosan grafted with graphene oxide | 60.4 | [8] |
| CuO–Al$_2$O$_3$ composite | 97.04 | [28] |
| MnFe$_2$O$_4$ | 497.5 | [14] |
| Amorphous Fe$_3$O$_4$ | 1,125 | [11] |
| Graphene | 1,520 | [7] |
| Amorphous CoO | 5,502 | [11] |
| ZnO nanoparticles | 7,918–9,198 | [13] |
| Amorphous NiO | 10,585 | [11] |

### 3.2.3. Adsorption kinetics

Adsorption kinetics is important in the treatment of aqueous effluents because it provides valuable information on the rate and mechanism of adsorption [30]. Fig. 6(a) shows the adsorption kinetics of MB onto NiO nanobelts obtained by batch adsorption studies at the initial MB concentration $C_0 = 300$ mg/L. It is found that the adsorption is very fast, and 76.9% of MB has been removed in the initial 10 min. And it reaches the adsorption equilibrium within 50 min. The high adsorption rate is beneficial to the practical application in wastewater treatment.

In order to investigate the adsorption kinetics, the pseudo-first-order and pseudo-second-order kinetic models are employed to analyze the experimental data. The pseudo-first-order model is usually applied to analyze the initial stage in an adsorption process. It can be expressed as [31]:

$$\ln(Q_e - Q_t) = \ln Q_e - k_1 t \tag{7}$$

While the pseudo-second-order model is expressed by [32]:

$$\frac{t}{Q_t} = \frac{1}{k_2 Q_e^2} + \frac{t}{Q_e} \tag{8}$$

In Eqs. (7) and (8), $Q_t$ is the adsorption capacity (mg/g) at time $t$ (min), and $k_1$ (1/min) and $k_2$ (g/(mg.min)) are the rate constant of pseudo-first-order and pseudo-second-order kinetics, respectively. The fitting results are plotted in Fig. 6(b). $Q_e$, $k_1$, and $k_2$ can be calculated from linear plots of $\ln(Q_e - Q_t)$ vs. $t$ and $t/Q_t$ vs. $t$, respectively. The calculated results are presented in Table 2. Compared with the pseudo-first-order kinetic model, the correlation coefficient $R^2$ of the pseudo-second-order kinetic model is higher (>0.99), and its $Q_{e,cal}$ is closer to the experimental value. Hence, the pseudo-second-order kinetic model is capable of describing the adsorption kinetics of MB, indicating that the adsorption of MB onto NiO nanobelts occurs in a chemical manner [33,34].

To obtain a deep understanding on the diffusion mechanism during the adsorption process, the intraparticle diffusion model presented by Webber is further applied to analyze the experimental data. The intraparticle diffusion model is expressed as [35]:

$$Q_t = K_t t^{1/2} + C \tag{9}$$

where $K_t$ is the intraparticle diffusion constant (mg/(g.min$^{1/2}$)), and $C$ is a constant providing the information about the thickness of the boundary layer, which can be obtained from the linear plot of $Q_t$ vs. $t^{1/2}$. The fitting plot of $Q_t$ vs. $t^{1/2}$ is shown in Fig. 7. It clearly exhibits three distinguishable intercepting linear portions, indicating two or more different stages take place. At the initial stage, the instantaneous adsorption or the adsorption on the external surface results in a sharp slope in the first linear portion due to the high initial MB concentration. Its deviation from the origin suggests that the intraparticle diffusion is not the sole rate-controlling step during the adsorption. Additional processes, such as the adsorption on the boundary layer, may also be involved in the control of the adsorption rate. Subsequently, the adsorption decelerates as a consequence of the decreased concentration gradient of MB between the solution and solid phase, as shown in the second linear portion, where the intraparticle diffusion is the rate-controlling region. Finally, the adsorption reaches the equilibrium, where the intraparticle diffusion decreases because of the low MB concentration in solution.

The values of $K_t$ and $C$ are determined from the slope and intercept of the linear portion and listed in Fig. 7. An order of $K_{t,1} > K_{t,2} > K_{t,3}$ is observed. Furthermore, the order of $C_3 > C_2 > C_1$ suggests an increase in the effect of the boundary layer [36]. Taken together, these findings further raise the possibility that the pseudo-second-order model adequately describes the adsorption of MB onto NiO nanobelts and that the intraparticle diffusion takes place in the adsorption process.

*3.3. The regeneration ability of NiO nanobelt*

It is known that the stability and regeneration ability of adsorbent is crucial to its practical application. The regeneration ability of NiO nanobelt was thus evaluated by performing the recycling experiment. Five consecutive adsorption–regeneration cycle experiments were carried out with the initial MB concentration kept at 300 mg/L. After an adsorption process, NiO nanobelts were separated by centrifugation and washed repeatedly with ethanol and deionized water under stirring for 30 min, and then dried at 80°C overnight for the next cycle adsorption [17]. Fig. 8 shows that the removal percentage of MB decreases from 95% to 91% after five consecutive cycles. These results reveal that NiO nanobelts can be easily regenerated and maintain good adsorption performance after being used for five cycles. Therefore, NiO nanobelt could be employed as a promising stable adsorbent for treatment of wastewater containing organic dyes.
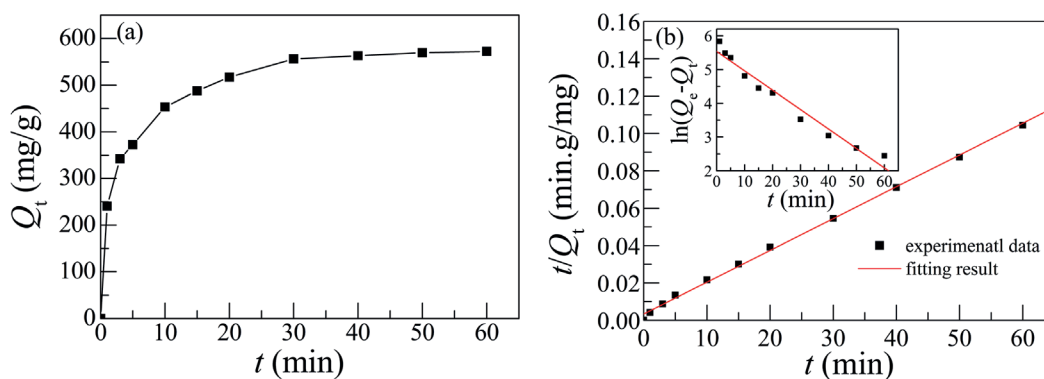


Fig. 6. (a) Variation of the adsorption capacity $Q_t$ with the adsorption time $t$ and (b) fitting results of pseudo-second-order kinetics and pseudo-first-order kinetics (inset): the initial MB concentration $C_0$ = 300 mg/L.

Table 2
Pseudo-first-order and pseudo-second-order kinetic parameters of MB adsorption on NiO nanobelts

| $C_0$ (mg/L) | $Q_{e,exp}$ (mg/g) | Pseudo-first-order kinetics | | | Pseudo-second-order kinetics | | |
|---|---|---|---|---|---|---|---|
| | | $Q_{e,cal}$ (mg/g) | $k_1$ (1/min) | $R^2$ | $Q_{e,cal}$ (mg/g) | $k_2$ (g/(mg.min)) | $R^2$ |
| 300 | 584.0 | 254.3 | $5.75 \times 10^{-2}$ | 0.964 | 588.2 | $8.60 \times 10^{-4}$ | 0.999 |

### 3.4. Mechanism of adsorption

In general, the adsorption capacity of an adsorbent depends on the property of adsorbate and surface property of the adsorbent since an adsorption occurs via the interaction between the adsorbate and the active sites of adsorbent. FT-IR studies could reveal the participation of the functional groups in the adsorption process.

The FT-IR spectra of MB, NiO nanobelts before and after MB adsorption, are shown in Fig. 9. Since the spectra in the region of 2,000–4,000 cm$^{-1}$ are almost unchanged after adsorption, thus, we only plot the spectra below 2,000 cm$^{-1}$. For MB, the peaks at 1,575, 1,495, and 1,449 cm$^{-1}$ are assigned to the aromatic ring vibrations. The C–N stretching vibration locates at 1,337 cm$^{-1}$. The peaks at 1,169, 1,121, 1,032, and 1,005 cm$^{-1}$ are attributed to the $SO_3^-$ radical vibrations [11]. The peak of C–N stretching vibration does not change after adsorption. And the peak intensity of aromatic ring vibrations becomes a little weaker compared with pure MB. However, for the $SO_3^-$ group, the peak at 1,005 cm$^{-1}$ almost disappears, and the peak at 1,032 cm$^{-1}$ is weakened. Moreover, the peaks at 1,121 and 1,169 cm$^{-1}$ of pure MB shift to lower wavenumber after adsorption. These results confirm that the adsorption of MB onto NiO nanobelts occurs by chemisorption between $SO_3^-$ group and positively charged surface of NiO.

### 3.5. Selective adsorption

Based on the above analysis of the adsorption mechanism, the selective adsorption of NiO nanobelt was further studied. To this end, two anionic dyes CR and MB, and two cationic dyes RhB and MYB, were selected. Table 3 lists their chemical structures, general data, and equilibrium adsorption capacities.

An isoelectric point of 10.8 was reported for NiO nanoparticles [40]. When the pH value of dye aqueous solution is below the isoelectric point, NiO will have a positive surface charge and would be expected to experience a significant electrostatic attraction with anionic dye molecules. For the above dye aqueous solutions, the pH value is 7.0–9.0; therefore, NiO possesses a positive surface charge. As we expect, the adsorption of NiO nanobelts is highly selective as that shown in Table 3. Under the same condition, the maximum adsorption capacity for MO and CR is 1,291 and 331 mg/g, respectively. The adsorption capacity for MB is the highest since MB contains three $SO_3^-$ groups. Whereas CR and MO have two $SO_3^-$ groups and one $SO_3^-$ group, respectively. Higher molecular weight and larger surface area (Table 3) are the probable reasons for the lower adsorption capacity of CR compared with MO. However, no $SO_3^-$ group exists in MYB and RhB, and they are cationic in aqueous solution, so MYB and RhB show a small adsorption capacity onto NiO nanbelts. Therefore, the good adsorption property of NiO nanobelt for MB, MO, and CR could be largely attributed to the electrostatic attraction between NiO positive surface charge and the anionic groups. Our NiO nanobelts exhibit much higher adsorption capacity for MO than other transition metal oxides reported previously (see Table 4). For the adsorption of CR, our product also show much better property compared with commercial NiO nanoparticles and NiO nanosheets, as listed in Table 5.
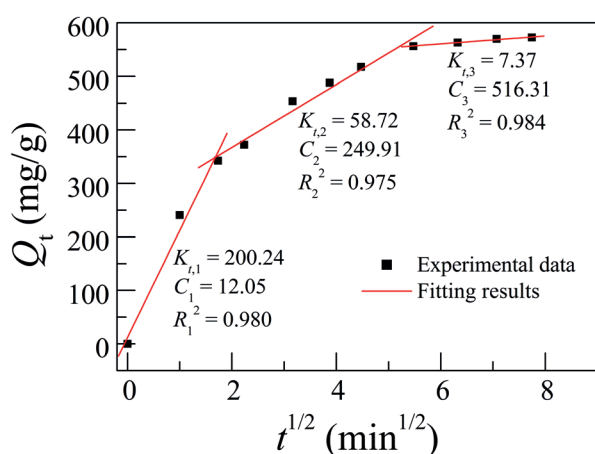


Fig. 7. Intraparticle diffusion model for MB adsorption onto NiO surface: the initial MB concentration $C_0$ = 300 mg/L.
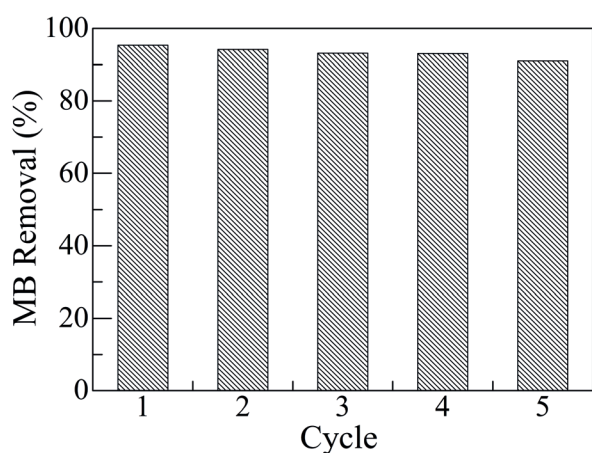


Fig. 8. Removal percentage of MB in five adsorption–regeneration cycles: the initial MB concentration $C_0$ = 300 mg/L.
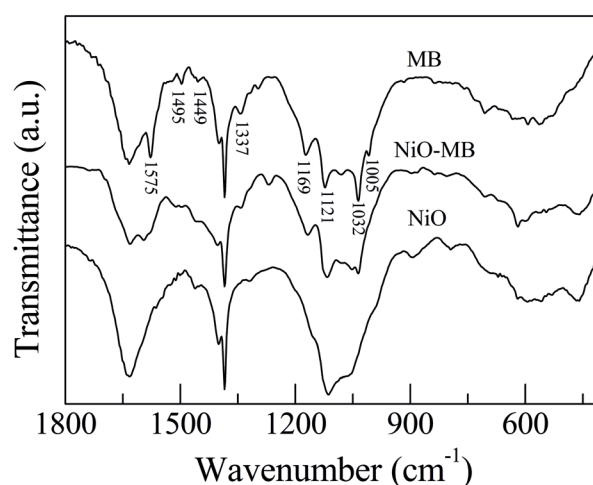


Fig. 9. FT-IR spectra of MB, NiO before and after adsorption of MB (NiO–MB): the initial MB concentration $C_0$ = 300 mg/L.

The adsorption capacity of adsorbent is dependent on the interaction between adsorbent and dye molecule, density of adsorption sites and function groups, specific surface area of adsorbent, as well as the dye structure. Adsorbent through ionic bonding generally shows a higher adsorption capacity than that through π–π bonding, hydrogen bond interaction, or van der Waals interaction between the adsorbent and dye molecule. Amorphous Fe, Co, and Ni oxides showed super adsorption capacity for removal of MB due to the strong ionic interaction (Table 3). And it was believed that the amorphization of Fe, Co, and Ni oxides provided much more active sites as adsorption sites and hung more function groups, which greatly promoted the adsorbing performance [11]. However, their adsorption capacity for MO drastically decreased (Table 4). The possible reason is that the number of $SO_3^-$ group in MO is smaller than that in MB. Bruneian peat and commercial NiO showed a relatively low adsorption capacity for CR (Table 5) maybe due to their low

**Table 3**
Chemical structures, general data, and equilibrium adsorption capacities of five dyes investigated in this work
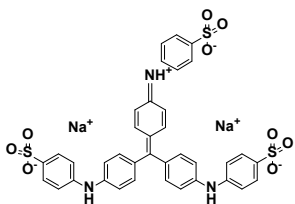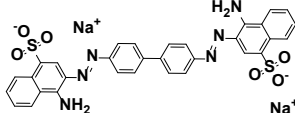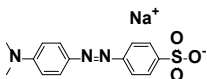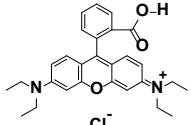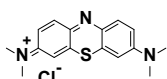
| Dye | Chemical structure | $\lambda_{max}$ (nm) | MW (g/mol) | Surface area (Å²) | $Q_e$ (mg/g) |
|---|---|---|---|---|---|
| MB | | 590 | 799.80 | 285 [37] | 1,996 |
| CR | | 500 | 696.66 | 558 [38] | 331 |
| MO | | 464 | 327.33 | 80 [39] | 1,291 |
| RhB | | 553 | 479.02 | 157 [39] | 19 |
| MYB | | 664 | 319.85 | 122 [37] | 76 |

**Table 4**
Comparison of adsorption results of MO onto some reported transition metal oxides

| Adsorbent | $Q_{max}$ (mg/g) | References |
|---|---|---|
| NiO nanobelts | 1,291 | This work |
| Amorphous $Fe_2O_3$ nanoparticles | 9.7 | [11] |
| Amorphous CoO nanoparticles | 11.5 | [11] |
| $\gamma$-$Fe_2O_3$/$SiO_2$/chitosan composite | 34.3 | [41] |
| Porous NiO microsphere | 164.7 | [12] |
| Amorphous NiO nanoparticles | 129.5 | [11] |
| Activated carbon/$NiFe_2O_4$ | 182.8 | [42] |
| Reduced graphene oxides modified Ni–Cr layered double hydroxides | 312.5 | [43] |
| $Fe_3O_4$/$Al_2O_3$/chitosan composite | 416.0 | [44] |
| Mesoporous $TiO_2$ | 454.5 | [15] |

**Table 5**
Comparison of the maximum adsorption capacity of CR onto various reported adsorbents

| Adsorbent | $Q_{max}$ (mg/g) | References |
|---|---|---|
| NiO nanobelts | 331 | This work |
| Bruneian peat | 10.1 | [45] |
| commercial NiO | 28 | [46] |
| NiO(111) nanosheets | 35.1 | [47] |
| Mesoporous $Fe_2O_3$ | 53 | [48] |
| NiO/graphene nanosheets | 123.9 | [49] |
| Hierarchical NiO nanosheets | 151.7 | [50] |
| NiO nanosheets | 167.7 | [51] |
| NiO nanosheets | 180 | [46] |
| NiO–$SiO_2$ hollow microspheres | 204.1 | [52] |
| Flower-like NiO architectures | 342.8 | [53] |
| NiO nanoflowers | 525 | [46] |
| Ag-doped Calcium hydroxyapatite | 554.5 | [54] |

specific surface area as well as the low concentration of effective adsorption sites [45,46].

From Table 5, we find that the adsorption capacity of adsorbent is dependent on the morphology of adsorbent. NiO nanosheets exhibited higher adsorption capacity for CR with 120~180 mg/g than commercial NiO [46,49–51]. While the adsorption capacities of NiO nanobelts and flower-like NiO [46,53] were even higher. Therefore, in addition to the specific surface area of adsorbent and the interaction between the adsorbent and adsorbate, the morphology of adsorbent also plays an important role in the adsorption activity of adsorbent.

## 4. Conclusions

In summary, NiO nanobelts are synthesized by a facile, template-free hydrothermal reaction, followed by calcination at 350°C. NiO nanobelts have a high specific surface area and exhibit an excellent adsorption capacity for anionic dyes including MB, MO, and CR. The adsorption of MB can be well described by Langmuir isotherm model. The adsorption kinetics follows the pseudo-second-order kinetic model, revealing the chemisorption nature. We find that the adsorption occurs through the electrostatic attraction between anionic dye molecule and NiO with positive surface charge. Our NiO nanobelts show much higher adsorption capacity for MO and CR compared with some other transition metal oxides and NiO nanosheets/nanoparticles reported previously. Therefore, our product is expected to be a very promising stable adsorbent for wastewater treatment.

## Acknowledgment

## References

[1] V.V. Panic, S.J. Velickovic, Removal of model cationic dye by adsorption onto poly(methacrylic acid)/zeolite hydrogel composites: kinetics, equilibrium study and image analysis, Sep. Purif. Technol., 122 (2014) 384–394.

[2] V.K. Gupta, Suhas, Application of low-cost adsorbents for dye removal – a review, J. Environ. Manage., 90 (2009) 2313–2342.

[3] G. Mezohegyi, F.P.V.D. Zee, J. Font, A. Fortuny, A. Fabregat, Towards advanced aqueous dye removal processes: a short review on the versatile role of activated carbon, J. Environ. Manage., 102 (2012) 148–164.

[4] C. He, X.J. Hu, Anionic dye adsorption on chemically modified ordered mesoporous carbons, Ind. Eng. Chem. Res., 50 (2011) 14070–14083.

[5] V. Selen, Ö. Güler, D. Özer, E. Evin, Synthesized multi-walled carbon nanotubes as a potential adsorbent for the removal of methylene blue dye: kinetics, isotherms, and thermodynamics, Desal. Wat. Treat., 57 (2016) 8826–8838.

[6] M.J. Iqbal, M.N. Ashiq, Adsorption of dyes from aqueous solutions on activated charcoal, J. Hazard. Mater., 139 (2007) 57–66.

[7] T. Wu, X. Cai, S.Z. Tan, H.Y. Li, J.S. Liu, W.D. Yang, Adsorption characteristics of acrylonitrile, p-toluenesulfonic acid, 1-naphthalenesulfonic acid and methyl blue on graphene in aqueous solutions, Chem. Eng. J., 173 (2011) 144–149.

[8] L.L. Fan, C.N. Luo, X.J. Li, F.G. Lu, H.M. Qiu, M. Sun, Fabrication of novel magnetic chitosan grafted with graphene oxide to enhance adsorption properties for methyl blue, J. Hazard. Mater., 215–216 (2012) 272–279.

[9] N.P. Raval, P.U. Shah, D.G. Ladha, P.M. Wadhwani, N.K. Shah, Comparative study of chitin and chitosan beads for the adsorption of hazardous anionic azo dye Congo red from wastewater, Desal. Wat. Treat., 57 (2016) 9247–9262.

[10] P. Phatai, C.M. Futalan, Removal of methyl violet dye by adsorption onto mesoporous mixed oxides of cerium and aluminum, Desal. Wat. Treat., 57 (2016) 8884–8893.

[11] L.H. Li, J. Xiao, P. Liu, G.W. Yang, Super adsorption capability from amorphousization of metal oxide nanoparticles for dye removal, Sci. Rep., 5 (2015) 9028.

[12] Z.G. Jia, J.H. Liu, Q.Z. Wang, M.F. Ye, R.S. Zhu, Facile preparation of mesoporous nickel oxide microspheres and their adsorption property for methyl orange from aqueous solution, Mater. Sci. Semicond. Process., 26 (2014) 716–725.

[13] F. Zhang, J. Lan, Y. Yang, T.F. Wei, R.Q. Tan, W.J. Song, Adsorption behavior and mechanism of methyl blue on zinc oxide nanoparticles, J. Nanopart. Res., 15 (2013) 2034.

[14] L.J. Yang, Y.Y. Zhang, X.Y. Liu, X.Q. Jiang, Z.Z. Zhang, T.T. Zhang, L. Zhang, The investigation of synergistic and competitive interaction between dye Congo red and methyl blue on magnetic $MnFe_2O_4$, Chem. Eng. J., 246 (2014) 88–96.

[15] S. Asuha, X.G. Zhou, S. Zhao, Adsorption of methyl orange and Cr(VI) on mesoporous $TiO_2$ prepared by hydrothermal method, J. Hazard. Mater., 181 (2010) 204–210.

[16] H. Liang, L. Liu, Z.J. Yang, Y.Z. Yang, Hydrothermal synthesis of ultralong single-crystalline $\alpha$-Ni(OH)$_2$ nanobelts and corresponding porous NiO nanobelts, Cryst. Res. Technol., 45 (2010) 661–666.

[17] F. Zhang, W.J. Song, J. Lan, Effective removal of methyl blue by fine-structured strontium and barium phosphate nanorods, Appl. Surf. Sci., 326 (2015) 195–203.

[18] P.V. Kamath, G.H.A. Therese, J. Gopalakrishnan, On the existence of hydrotalcite-like phases in the absence of trivalent cations, J. Solid State Chem., 128 (1997) 38–41.

[19] D.N. Yang, R.M. Wang, J. Zhang, Z.F. Liu, Synthesis of nickel hydroxide nanoribbons with a new phase: a solution chemistry approach, J. Phys. Chem. B, 108 (2004) 7531–7533.

[20] T. Gao, B.P. Jelle, Paraotwayite-type $\alpha$-Ni(OH)$_2$ nanowires: structural, optical, and electrochemical properties, J. Phys. Chem. C, 117 (2013) 17294–17302.

[21] Y.W. Tang, Z.Y. Jia, Y. Jiang, L.Y. Li, J.B. Wang, Simple template-free solution route for the synthesis of Ni(SO$_4$)$_{0.3}$(OH)$_{1.4}$ nanobelts and their thermal degradation, Nanotechnology, 17 (2006) 5686–5690.

[22] W.Z. Wang, W.W. Zhang, C.C. Hao, F. Wu, Y.J. Liang, H.L. Shi, J. Wang, T. Zhang, Y.Q. Hua, Enhanced photoelectrochemical activity and photocatalytic water oxidation of NiO nanoparticle-decorated SrTiO$_3$ nanocube heterostructures: interaction, interfacial charge transfer and enhanced mechanism, Sol. Energy Mater. Sol. Cells, 152 (2016) 1–9.

[23] Y. Hattori, T. Konishi, K. Kaneko, XAFS and XPS studies on the enhancement of methane adsorption by NiO dispersed ACF with the relevance to structural change of NiO, Chem. Phys. Lett., 355 (2002) 37–42.

[24] D.L. Legrand, H.W. Nesbitt, G.M. Bancroft, X-ray photoelectron spectroscopic study of a pristine millerite (NiS) surface and the effect of air and water oxidation, Am. Mineral., 83 (1998) 1256–1265.

[25] M.K. Younes, A. Ghorbel, A. Rives, R. Hubaut, Study of acidity of aerogels ZrO$_2$-SO$_4^{2-}$ by isopropanol dehydration reaction, surface potential and X-ray photoelectron spectroscopy, J. Sol-Gel Sci. Technol., 19 (2000) 817–819.

[26] L. Ruangchuay, J. Schwank, A. Sirivat, Surface degradation of $\alpha$-naphthalene sulfonate-doped polypyrrole during XPS characterization, Appl. Surf. Sci., 199 (2002) 128–137.

[27] Y.F. Zhao, X.D. Jia, G.B. Chen, L. Shang, G.I.N. Waterhouse, L.Z. Wu, C.H. Tung, D. O'Hare, T.R. Zhang, Ultrafine NiO nanosheets stabilized by $TiO_2$ from monolayer NiTi-LDH precursors: an active water oxidation electrocatalyst, J. Am. Chem. Soc., 138 (2016) 6517–6524.

[28] N.J. Duan, Q.R. Li, J. Liu, H.Y. Xiao, Enhanced adsorption performance of CuO-Al$_2$O$_3$ composite derived from cotton template, Can. J. Chem. Eng., 93 (2015) 2015–2023.

[29] I. Langmuir, The adsorption of gases on plane surfaces of glass, mica and platinum, J. Am. Chem. Soc., 40 (1918) 1361–1403.

[30] H. Freundlich, Concerning the adsorption in solution, J. Phys. Chem., 57 (1906) 385–471.

[31] M.I. El-Khaiary, G.F. Malash, Common data analysis errors in batch adsorption studies, Hydrometallurgy, 105 (2011) 314–320.

[32] Y.S. Ho, G. McKay, Sorption of dye from aqueous solution by peat, Chem. Eng. J., 70 (1998) 115–124.

[33] I.A.W. Tan, A.L. Ahmad, B.H. Hameed, Adsorption isotherms, kinetics, thermodynamics and desorption studies of 2,4,6-trichlorophenol on oil palm empty fruit bunch-based activated carbon, J. Hazard. Mater., 164 (2009) 473–482.

[34] W.H. Zou, K. Li, H.J. Bai, X.L. Shi, R.P. Han, Enhanced cationic dyes removal from aqueous solution by oxalic acid modified rice husk, J. Chem. Eng. Data, 56 (2011) 1882–1891.

[35] Y.S. Ho, G. McKay, Pseudo-second order model for sorption processes, Process Biochem., 34 (1999) 451–465.

[36] G.K. Ramesha, A.V. Kumara, H.B. Muralidhara, S. Sampath, Graphene and graphene oxide as effective adsorbents toward anionic and cationic dyes, J. Colloid Interface Sci., 361 (2011) 270–277.

[37] R. Ocampo-Pérez, R. Leyva-Ramos, M. Sanchez-Polo, J. Rivera-Utrilla, Role of pore volume and surface diffusion in the adsorption of aromatic compounds on activated carbon, Adsorption, 19 (2013) 945–957.

[38] Z.L. Yaneva, N.V. Georgieva, Insights into Congo red adsorption on agro-industrial materials – spectral, equilibrium, kinetic, thermodynamic, dynamic and desorption studies. A review, Int. Rev. Chem. Eng., 4 (2012) 127–146.

[39] J.H. Huang, K.L. Huang, S.Q. Liu, A.T. Wang, C. Yan, Adsorption of Rhodamine B and methyl orange on a hypercrosslinked polymeric adsorbent in aqueous solution, Colloids Surf., A: Physicochem. Eng. Asp., 330 (2008) 55–61.

[40] L. Xiang, X.Y. Deng, Y. Jin, Experimental study on synthesis of NiO nano-particles, Scr. Mater., 47 (2002) 219–224.

[41] H.Y. Zhu, R. Jiang, Y.Q. Fu, J.H. Jiang, L. Xiao, G.M. Zeng, Preparation, characterization and dye adsorption properties of $\gamma$-Fe$_2$O$_3$/SiO$_2$/chitosan composite, Appl. Surf. Sci., 258 (2011) 1337–1344.

[42] T. Jiang, Y.D. Liang, Y.J. He, Q. Wang, Activated carbon/NiFe$_2$O$_4$ magnetic composite: a magnetic adsorbent for the adsorption of methyl orange, J. Environ. Chem. Eng., 3 (2015) 1740–1751.

[43] X.X. Ruan, Y.H. Chen, H. Chen, G.R. Qian, R.L. Frost, Sorption behavior of methyl orange from aqueous solution on organic matter and reduced graphene oxides modified Ni–Cr layered double hydroxides, Chem. Eng. J., 297 (2016) 295–303.

[44] B. Tanhaei, A. Ayati, M. Lahtinen, M. Sillanpää, Preparation and characterization of a novel chitosan/Al$_2$O$_3$/magnetite nanoparticles composite adsorbent for kinetic, thermodynamic and isotherm studies of methyl orange adsorption, Chem. Eng. J., 259 (2015) 1–10.

[45] T. Zehra, N. Priyantha, L.B.L. Lim, E. Iqbal, Sorption characteristics of peat of Brunei Darussalam V: removal of Congo red dye from aqueous solution by peat, Desal. Wat. Treat., 54 (2015) 2592–2600.

[46] L.X. Song, Z.K. Yang, Y. Teng, J. Xia, P. Du, Nickel oxide nanoflowers: formation, structure, magnetic property and adsorptive performance towards organic dyes and heavy metal ions, J. Mater. Chem. A, 1 (2013) 8731–8736.

[47] Z. Song, L.F. Chen, J.C. Hu, R. Richards, NiO(111) nanosheets as efficient and recyclable adsorbents for dye pollutant removal from wastewater, Nanotechnology, 20 (2009) 275707.

[48] C.C. Yu, X.P. Dong, L.M. Guo, J.T. Li, F. Qin, L.X. Zhang, J.L. Shi, D.S. Yan, Template-free preparation of mesoporous Fe$_2$O$_3$ and its application as absorbents, J. Phys. Chem. C, 112 (2008) 13378–13382.

[49] X.S. Rong, F.X. Qiu, J. Qin, H. Zhao, J. Yan, D.Y. Yang, A facile hydrothermal synthesis, adsorption kinetics and isotherms to Congo red azo-dye from aqueous solution of NiO/graphene nanosheets adsorbent, J. Ind. Eng. Chem., 26 (2015) 354–363.

[50] B. Cheng, Y. Le, W.Q. Cai, J.G. Yu, Synthesis of hierarchical Ni(OH)$_2$ and NiO nanosheets and their adsorption kinetics and isotherms to Congo red in water, J. Hazard. Mater., 185 (2011) 889–897.

[51] J.F. Zhao, Y. Tan, K. Su, J.J. Zhao, C. Yang, L.L. Sang, H.B. Lu, J.H. Chen, A facile homogeneous precipitation synthesis of NiO nanosheets and their applications in water treatment, Appl. Surf. Sci., 337 (2015) 111–117.

[52] C.S. Lei, X.F. Zhu, B.C. Zhu, J.G. Yu, W.K. Ho, Hierarchical NiO–SiO$_2$ composite hollow microspheres with enhanced adsorption affinity towards Congo red in water, J. Colloid Interface Sci., 466 (2016) 238–246.

[53] H.M. Hu, G.Y. Chen, C.H. Deng, Y. Qian, M. Wang, Q. Zheng, Green microwave-assisted synthesis of hierarchical NiO architectures displaying a fast and high adsorption behavior for Congo red, Mater. Lett., 170 (2016) 139–141.

[54] C. Srilakshmi, R. Saraf, Ag-doped hydroxyapatite as efficient adsorbent for removal of Congo red dye from aqueous solution: synthesis, kinetic and equilibrium adsorption isotherm analysis, Microporous Mesoporous Mater., 219 (2016) 134–144.